High-throughput, combinatorial synthesis of multimetallic nanoclusters

Yonggang Yao[a,1], Zhennan Huang[b,1], Tangyuan Li[a,1], Hang Wang[c,1], Yifan Liu[d], Helge S. Stein[e], Yimin Mao[a,f], Jinlong Gao[a], Miaolun Jiao[a], Qi Dong[a], Jiaqi Dai[a], Pengfei Xie[d], Hua Xie[a], Steven D. Lacey[a], Ichiro Takeuchi[a], John M. Gregoire[e], Rongzhong Jiang[g,2], Chao Wang[e,2], Andre D. Taylor[c,2], Reza Shahbazian-Yassar[b,2], and Liangbing Hu[a,2]

[a]Department of Materials Science and Engineering, University of Maryland, College Park, MD 20742; [b]Department of Mechanical and Industrial Engineering, University of Illinois at Chicago, Chicago, IL 60607; [c]Department of Chemical and Biomolecular Engineering, New York University, Brooklyn, NY 11201; [d]Department of Chemical and Biomolecular Engineering, Johns Hopkins University, Baltimore, MD 21218; [e]Joint Center for Artificial Photosynthesis, California Institute of Technology, Pasadena, CA 91125; [f]Center for Neutron Research, National Institute of Standards and Technology, Gaithersburg, MD 20899; and [g]Sensors and Electron Devices Directorate, Combat Capabilities Development Command Army Research Laboratory, Adelphi, MD 20783

Edited by Catherine J. Murphy, University of Illinois Urbana–Champaign, Urbana, IL, and approved February 6, 2020 (received for review March 8, 2019)

Multimetallic nanoclusters (MMNCs) offer unique and tailorable surface chemistries that hold great potential for numerous catalytic applications. The efficient exploration of this vast chemical space necessitates an accelerated discovery pipeline that supersedes traditional "trial-and-error" experimentation while guaranteeing uniform microstructures despite compositional complexity. Herein, we report the high-throughput synthesis of an extensive series of ultrafine and homogeneous alloy MMNCs, achieved by 1) a flexible compositional design by formulation in the precursor solution phase and 2) the ultrafast synthesis of alloy MMNCs using thermal shock heating (i.e., ∼1,650 K, ∼500 ms). This approach is remarkably facile and easily accessible compared to conventional vapor-phase deposition, and the particle size and structural uniformity enable comparative studies across compositionally different MMNCs. Rapid electrochemical screening is demonstrated by using a scanning droplet cell, enabling us to discover two promising electrocatalysts, which we subsequently validated using a rotating disk setup. This demonstrated high-throughput material discovery pipeline presents a paradigm for facile and accelerated exploration of MMNCs for a broad range of applications.

combinatorial | high-throughput synthesis | multimetallic nanoclusters | thermal shock | oxygen reduction reaction

Nanoparticles with a range of sizes and morphologies have been extensively studied for various catalytic applications; however, most nanoparticles studied comprise three or fewer elements to avoid synthetic complexity and structural heterogeneity (1–7). Multimetallic nanoclusters (MMNCs; i.e., ultrafine nanoparticles with ≥3 elements) represent a vast and largely undiscovered chemical space that promised to tune material properties via high-dimensional composition control and the associated synergistic interactions among different elements (8–16). However, with increasing compositional complexity, conventional synthetic methods often lead to MMNCs with wider size distribution and inhomogeneous structures (e.g., phase separation and/or elemental segregation inside the particles). These inhomogeneities originate from the substantial challenge in controlling the kinetics and dynamics of chemical reactions at the nanoscale among these dissimilar constituents (1, 4–6, 10–12, 14, 17). The size and structural heterogeneity make it formidable to controllably tune the composition and systematically study MMNCs, thus limiting material discovery, property optimization, and mechanistic understanding for different functionalities.

Additionally, with the increased number of components, the resulting combinatorial explosion in the composition space would necessitate significant investment in MMNC synthesis and screening, posing a great challenge to traditional methods, which are typically slow (one sample or less per day) and compositionally specific (i.e., processing parameters are not generally applicable to different compositions). In contrast to sample-by-sample trial and error, the adoption of a high-throughput paradigm can provide the parallel synthesis of a large number of samples featuring different compositions, saving both time and effort (18–27). Pioneering works have demonstrated the combinatorial synthesis of various heterogeneous catalysts (having three to five elements) using either thin-film deposition techniques or spatially confined tip syntheses (20, 21, 23, 25, 27–29). However, the uniformity of the synthesized gradient library, especially in terms of structure, is often lacking or has been insufficiently studied, making it difficult to compare among their catalytic performances.

In this work, we report the high-throughput synthesis and screening of a series of ultrafine and alloyed MMNCs supported on surface-treated carbon supports in the PtPdRhRuIrFeCoNi space. The high-throughput synthesis is achieved by combinatorial composition formulation in the solution phase, followed by

Significance

Multielement nanomaterials hold great promise for various applications due to their widely tunable surface chemistry, yet it remains challenging to efficiently study this multidimensional space. Conventional approaches are typically slow and depend on serendipity, while a robust and general synthesis is still lacking among increasingly complex compositions. We report a high-throughput technique for combinatorial compositional design (formulation in solution phases) and rapid synthesis (within seconds) of ultrafine multimetallic nanoclusters with a homogeneous alloy structure. We synthesized and screened the PtPdRhRuIrFeCoNi compositional space using scanning droplet cell electrochemistry, with two promising catalysts quickly identified and further verified in a rotating disk setup. The reported high-throughput approach establishes a facile and reliable pipeline to significantly accelerate material discovery in multimetallic nanomaterials.

Author contributions: Y.Y. and L.H. designed research; Y.Y., Z.H., T.L., H.W., Y.L., Y.M., J.G., M.J., Q.D., P.X., H.X., S.D.L., and R.J. performed research; Z.H., H.S.S., Y.M., J.D., J.M.G., and R.S.-Y. contributed new reagents/analytic tools; Y.Y., T.L., H.W., Y.L., H.S.S., Y.M., J.G., M.J., Q.D., P.X., I.T., J.M.G., R.J., C.W., A.D.T., R.S.-Y., and L.H. analyzed data; Y.Y. and L.H. wrote the paper; and T.L., I.T., C.W., A.D.T., and R.S.-Y. revised the manuscript.

The authors declare no competing interest.

This article is a PNAS Direct Submission.

[1]Y.Y., Z.H., T.L., and H.W. contributed equally to this work.

[2]To whom correspondence may be addressed. Email: rongzhong.jiang.civ@mail.mil, chaowang@jhu.edu, adt4@nyu.edu, rsyassar@uic.edu, or binghu@umd.edu.

This article contains supporting information online at https://www.pnas.org/lookup/suppl/doi:10.1073/pnas.1903721117/-/DCSupplemental.

First published March 10, 2020.

a rapid thermal-shock treatment. In the process, the surface defects on the carbon help to disperse the MMNCs and ensure their size uniformity among the compositionally different samples, while the rapid shock process leads to the single-phase structure due to high-temperature mixing and fast quenching. These compositionally different MMNCs (with similar size and structure) were rapidly screened by using scanning droplet cell analysis for the electrochemical oxygen reduction reaction (ORR), enabling us to quickly identify the two best-performing catalysts. We also verified these two optimized MMNC catalysts in a prototypical rotating disk setup and compared their performance with a Pt control sample. Our combinatorial and high-throughput approach, therefore, paves the way for the rapid synthesis and compositional exploration of MMNCs as advanced catalytic materials.

Results

Conventionally, vapor-phase depositions can create a large number of samples using composition gradient; however, they require sophisticated and expensive equipment with a limited choice of materials and substrates (typically wafers; Fig. 1*A*). In contrast, the reported high-throughput synthesis involves two facile steps: 1) combinatorial composition design using metal precursors by formulation in solution phases, which is remarkably facile and easily accessible; and 2) uniform MMNC synthesis by rapid thermal shock of precursor-loaded carbon support, which drives the rapid precursor decomposition and alloy formation (Fig. 1*B*).

As a demonstration, we synthesized a series of MMNCs, from ternary (PtPdRh) to octonary (PtPdRhRuIrFeCoNi) materials, by adding one element at a time (Fig. 1*B*). The salt precursors were individually dissolved (0.05 mol/L) and printed onto the suspended carbon nanofiber (CNF) films by a programmable printer, taking only minutes to complete (Movie S1). The printed precursor mixture shows a homogeneous and uniform precursor distribution on the carbon substrates, proved via energy-dispersive spectroscopy (EDS) mapping (Fig. 1*C* for PtPdRh and *SI Appendix*, Figs. S1 and S2 for PtPdRhRuIr and PtPdRhRuIrFeCoNi). The initial homogeneity of the formulated precursors is important for subsequent particle uniformity. The precursor-loaded carbon supports were then subjected to high-temperature thermal shock, demonstrated by electrically Joule heating to ∼1,650 K for a duration of ∼500 ms (*SI Appendix*, Figs. S3 and S4). The samples can be electrically connected in series for batch thermal shocking or heated individually. In either case, the shock heating induced the rapid decomposition of precursors and the formation of uniformly dispersed nanoparticles.

Fig. 1 *D*–*F* show the ultrasmall and uniform distribution of PtPdRh, PtPdRhRuIr, and PtPdRhRuIrFeCoNi MMNCs, revealing their similar size and dispersity, despite the compositional

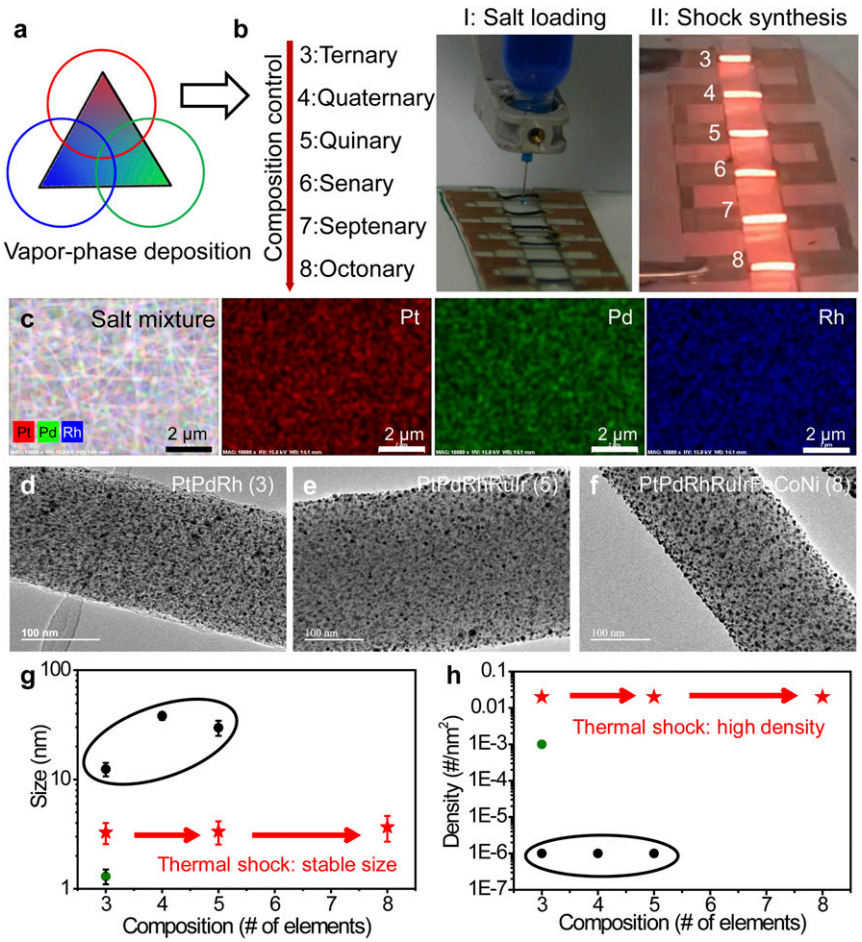

Fig. 1. (*A*) Schematic of a vapor-phase deposition method. (*B*) The high-throughput synthesis of MMNCs. Step I: combinatorial composition design in the liquid phase and then deposition on carbon supports; step II: rapid thermal shock synthesis (∼1,650 K, 500 ms). (*C*) EDS maps of the ternary salt mixture containing Pt, Pd, and Rh on the carbon support, demonstrating the uniform precursor loading. (*D*–*F*) TEM images demonstrating the similar size distribution and dispersal density of the ternary (PtPdRh), quinary (PtPdRhRuIr), and octonary (PtPdRhRuIrFeCoNi) MMNCs. (*G* and *H*) MMNCs synthesized by thermal shock in comparison with literature values in terms of size distribution and dispersal density [red stars, thermal shock; black dots, probe lithography (10, 34); green dots, macromolecular template method (8)].

differences. In the MMNC synthesis, the carbon support, made of CO_2-activated CNFs (CA-CNFs), plays a key role in enabling the ultrafine and uniform particle dispersion as compared with untreated CNFs (*SI Appendix*, Figs. S5 and S6). The CO_2-activation process increases the surface-defect concentration of the CA-CNFs, and these defects act as nucleation sites for uniform particle dispersion (30–33). *SI Appendix*, Fig. S7 further demonstrates the high-resolution, high-angle annular dark-field (HAADF) images of the three MMNCs and their corresponding size distributions: 3.3 ± 0.8, 3.4 ± 0.7, and 3.7 ± 1 nm, respectively, confirming very similar size distribution among compositionally different samples.

We also compared the size and particle-dispersion density of the MMNCs synthesized by the thermal-shock method with those reported in the literature, which have mainly been fabricated by advanced probe lithography (physical method) and macromolecular-template techniques (chemical control) (Fig. 1 *G* and *H*). Since particles composed of more than five elements have not yet been synthesized by other methods, we chose the ternary, quaternary, and quinary nanoparticles for comparison. Typical ternary, quaternary, and quinary MMNCs synthesized by probe lithography feature a size distribution of 12.4 ± 1.8, 38.1 ± 3.1, and 30.0 ± 4.7 nm, respectively, with a patterning density of $1/\mu m^2$ (i.e., $1 \times 10^{-6}/nm^2$) on a flat surface (10, 34). While much smaller MMNCs ($\sim 1.3 \pm 0.2$ nm) can be synthesized by using the macromolecular template method, the dispersion density is quite low ($1 \times 10^{-3}/nm^2$), and the composition of choice is also limited (8). In the thermal-shock synthesis on defective carbon supports, both the size and dispersal density remain similar for MMNCs with various compositions. The uniform size and dispersity are critical to ensure later comparative study among these MMNCs.

For conventional synthesis methods, incorporating more elements typically results in heterogeneous structures, due to the immiscibility among different elements (5, 10, 11, 13). The thermal-shock method could overcome this immiscibility by creating liquid metal-alloy states at high temperature, followed by rapid quenching to largely maintain the alloy mixing (35). In addition, the multielement materials could help drive the alloy formation through increasing entropy ($\Delta G_{mix}\downarrow = \Delta H_{mix} - T^*\Delta S_{mix}\uparrow$), and the increased entropy also provides kinetical constraints (severe lattice distortion and sluggish diffusion) so as to stabilize the alloy structures against phase separation (17, 36). Please note that immiscible combinations with a low mixing entropy (fewer elements or composition ratios largely deviate from equal mixing) could lead to phase separation, even synthesized at a high temperature (36).

We have studied the detailed structures of these MMNCs using HAADF and EDS mapping (Fig. 2). Low-magnification HAADF and EDS maps confirmed the ultrafine size and high-density dispersion of the nanoclusters, with each element roughly distributed throughout the fiber support without obvious elemental segregation (Fig. 2*A*). High-resolution HAADF and EDS images of the ternary (Fig. 2*B* and *SI Appendix*, Fig. S8), quinary (Fig. 2*C* and *SI Appendix*, Fig. S9), and octonary (Fig. 2*D* and *SI Appendix*, Fig. S10) samples show ~3- to 4-nm particles with each element uniformly distributed within each nanocluster without clear phase separation or elemental segregation, indicating a solid-solution structure, as hypothesized. The corresponding EDS profiles and energy intervals to differentiate each element are included in *SI Appendix*, Figs. S8–S11. Note that the final compositions in the MMNCs may be slightly varied from the initial design, largely due to the differences in metal-vapor pressures at high temperatures (35). The thermal-shock method enables alloying at high temperatures, while limiting the heating duration so as to minimize the metal losses.

Macroscopically, the powder X-ray diffraction (XRD) profiles (Fig. 2*E*) reveal an overall face-centered-cubic (FCC) structure for ternary, quinary, and octonary MMNCs by using the Rietveld refinement with a fitted lattice constant of 3.87, 3.82, and 3.76 Å, respectively. No obvious secondary phases were detected. The decreasing lattice constant was due to the increasing ratio of nonnoble metals (e.g., Fe, Co, and Ni) with a smaller size and lattice constant. In addition, we performed synchrotron XRD to detect the fine structure and possible impurity phases in the MMNCs using a much smaller wavelength ($\lambda = 0.2113$ Å). As shown in Fig. 2*F*, all of the major peaks can be indexed according to the FCC structure and a fitted lattice constant of 3.87 Å using Rietveld refinement with a reasonable good fit. Namely, the PtPdRh MMNCs still exhibited a largely single FCC phase under synchrotron detection, further confirming the single-phase alloy structure. Note that we converted the diffraction data using q unit, where $q = (4\pi\backslash\lambda)\sin\theta$, so that the data were comparable in the q unit regardless of the difference in X-ray energy. The solid-solution formation and alloy structural consistency of these MMNCs are critical for comparative catalytic studies.

From a high-throughput perspective, the overall MMNC synthesis protocol involves only printing precursor salts and rapid thermal shock, which are all physical processes that can be easily scaled up (Fig. 3*A*). First, different metal-salt solutions with desired recipes were well mixed in the liquid phase and deposited on the CA-CNF disks (~0.3-inch diameter, 5 μmol/cm^2 loading) and patterned on the copper plate. Then, rapid radiative heating (nondirect contact) was used for the MMNC synthesis by positioning a high-temperature heating source above the samples (~0.5 cm) and repeatedly shock heating (2,000 K, ~0.5 s) three times (*SI Appendix*, Fig. S12). Fig. 3 *B*, *Inset* displays an image of the plate containing a library of 88 samples, including 1) MMNCs in the PtPdRhRuIrFeCoNi compositional space for ORR; and 2) MMNCs in the IrRuAuPdMnFeCoNi space for the oxygen evolution reaction (OER), with each composition having two samples for cross-validation (compositions are listed in *SI Appendix*, Table S1). We also verified the single phase structure and uniform size distributions of selected MMNCs, as expected (*SI Appendix*, Fig. S13).

We then performed high-throughput electrochemistry using a scanning droplet cell setup to rapidly screen for promising MMNC catalysts. Scanning droplet cell analysis is used as a high-throughput electrochemical screening method for the rapid identification of active electrocatalysts (37–39). It integrates an ordinary three-electrode setup into a single tip (0.785 mm^2) (39) for fast, continuous, and even automatic screening. Here, the copper plate acts as the common current collector from working electrodes during the fast screening. Herein, we used ORR as a model reaction to illustrate one potential implementation of the rapid-catalysts screening process. ORR is a common cathode reaction to enable fuel-cell technologies for clean-energy applications, yet it is kinetically sluggish with a high overpotential, owing to the four-electron transfer process. Therefore, discovering high performance, low cost, and robust catalysts is critical to facilitate ORR and fuel-cell operation in a more efficient manner (16, 19, 34).

Fig. 3*B* shows the schematic of the scanning droplet cell setup, where the tip head and the ORR process are highlighted. The utilization of the scanning droplet cell configuration not only expedited the screening process but also ensured the evaluation of catalytic activity for all samples under comparable testing conditions. Note that our IrRu-based MMNC samples for OER were found to have apparent corrosion current at high potential, which can obscure the performance and cause uncertainty. Therefore, in the following discussion, we will focus on the PtPd-based compositions for ORR. As shown in Fig. 3*C*, linear sweep voltammetry (from 1.1 to 0.45 V) and cyclic voltammetry for different MMNC samples were performed in 0.1 M KOH at a scan rate of 5 mV/s to compare their activity and stability (*SI Appendix*, Table S2). Notably, the blank sample showed very weak activity toward ORR, which is in agreement with other reported results (40). The control Pt sample exhibited a good ORR catalytic activity, achieving -3×10^{-4} A at 0.45 V vs. the reversible hydrogen electrode (RHE). For the MMNC samples, while all

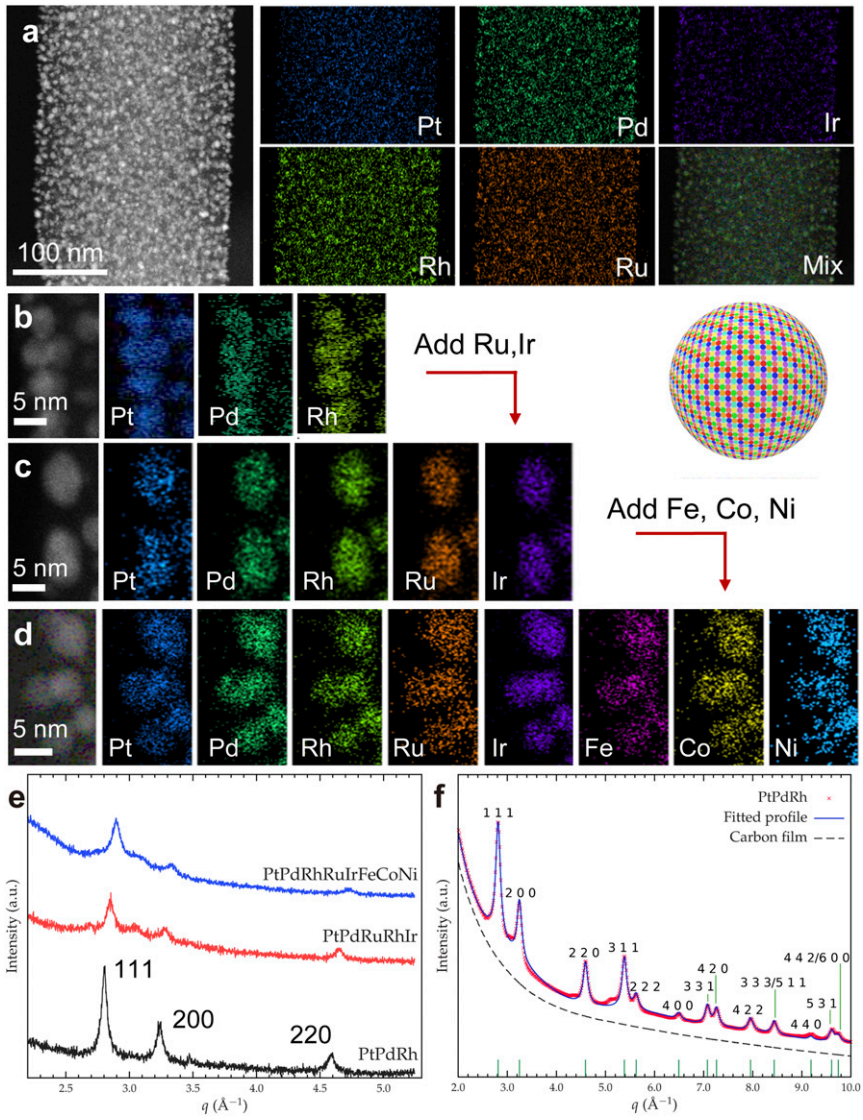

Fig. 2. Combinatorial synthesis of MMNCs featuring a solid-solution structure. (*A*) Low-magnification HAADF and EDS maps of quinary MMNCs (PtPdRhRuIr), demonstrating the uniform distribution of each element across the CA-CNF support. (*B–D*) High-resolution HAADF images and EDS maps of ternary, quinary, and octonary MMNCs demonstrating the uniform/homogeneous distribution of each element within the resulting nanoclusters. (Scale bars: 5 nm.) (*E*) Powder XRD measurement for ternary, quinary, and octonary MMNCs, showing the single-phase FCC structure without obvious secondary phases. (*F*) The synchrotron XRD (λ = 0.2113 Å) profile of PtPdRh still exhibits a single-phase FCC structure, with a lattice constant of 3.87 Å. a.u., arbitrary units.

shared a low onset potential similar to the Pt control, PtPdRhNi and PtPdFeCoNi showed a much larger current at a given potential than others, indicating higher activity. Note that for all samples, the current continued to increase as the potential decreased without showing a limiting current plateau. This is because relatively excessive oxygen was fed to the catalyst, so the reaction was not limited by oxygen mass transfer.

Fig. 3*D* summarizes the specific current at 0.45 V of different samples and reconstructed into a neural network diagram (data in *SI Appendix*, Fig. S14 and Table S2), where the size of the circles represents the magnitude of the sample's specific current at 0.45 V, while the lines indicate the connections between compositions. Although there is no obvious clue on the composition–performance relationship, these results are of great value for future data mining or machine-learning processes to uncover the hidden relationships on the elemental contributions to the catalytic performances and eventually guide the material design for accelerate catalyst discovery in MMNCs. We also verified the result with the other half-batch of samples having the same compositions (*SI Appendix*, Fig. S15).

To gain further insights into these two best-performing catalysts, we used both macroscale and microscale techniques for their structural characterization. As shown in Fig. 3*E*, the synchrotron XRD profiles of these two MMNCs (PtPdRhNi and PtPdFeCoNi) exhibit a single-phase FCC structure under synchrotron detection (λ = 0.2113 Å), with a fitted lattice constant of 3.78 and 3.73 Å, respectively, which is very similar to the powder diffraction data (*SI Appendix*, Fig. S16). We also verified the size distribution of the MMNCs as well as their alloy structure at the microscopic level (Fig. 3 *F* and *G*): The size remained small and uniformly distributed, while each element was distributed homogeneously throughout the nanoparticles, confirming the alloy structure at the nanoparticle level. The synchrotron XRD and TEM data verified the small size and single-phase alloy structure of the MMNCs synthesized by using the high-throughput thermal shock method.

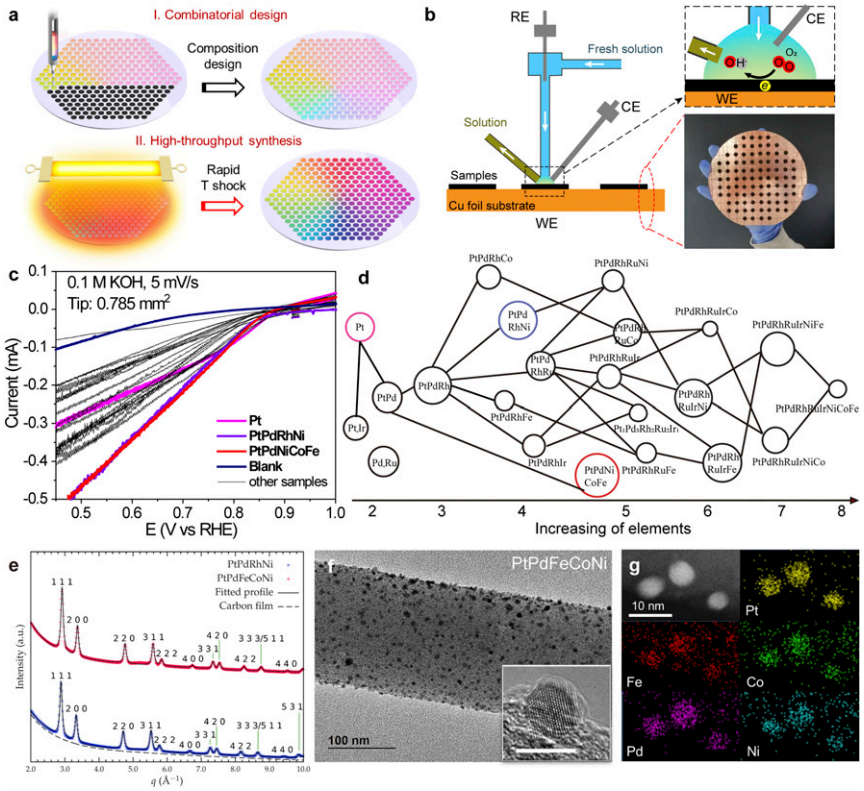

Fig. 3. Scale-up synthesis and fast screening of MMNCs for electrocatalytic reactions. (*A*) Schematic illustration of the combinatorial and high-throughput synthesis of uniform MMNCs. (*B*) The scanning droplet cell setup and patterned samples on the copper substrate. CE, counter electrode; RE, reference electrode; WE, working electrode. (*C*) Fast screening of PtPd-based MMNCs for catalytic ORR (22 compositions + 1 blank, 0.1 M KOH, 5 mV/s scan rate). (*D*) The compositional designs and their corresponding ORR performances presented in a neural network diagram. The size of the circles represents the magnitude of the specific current at 0.45 V for ORR. (*E*) Synchrotron XRD profiles for PtPdRhNi and PtPdFeCoNi, showing the single-phase FCC structure. a.u., arbitrary units. (*F* and *G*) TEM image (*F*) and elemental maps (*G*) of PtPdFeCoNi with uniform small size and alloy structure. *F*, *Inset* is a high-resolution TEM image of PtPdFeCoNi. (Scale bar: 5 nm.)

To verify the high performance of the two optimized catalysts (PtPdRhNi and PtPdFeCoNi), we then carried out electrochemical analysis using a conventional rotating disk electrode (RDE) setup (41, 42). Detailed electrode preparation and electrochemical testing can be found in *Methods*. Fig. 4*A* showcases the cyclic voltammograms of the PtPdRhNi and PtPdFeCoNi MMNCs and a Pt control sample (10 wt% loading) in an oxygen-saturated electrolyte (1 M KOH). A sharp peak evolved at ~0.85 V for all three samples, which corresponded to the reduction of oxygen. The peak positions of the MMNC catalysts were slightly positive compared with that of Pt as a control, indicating their lower overpotentials and therefore better catalytic activity. In addition, both MMNC catalysts exhibited increased peak current densities by approximately twofold that of Pt. In Fig. 4*B*, linear sweep voltammograms of the MMNC catalysts display flat limiting current densities with much higher values and slightly more positive half-wave potentials compared to that of Pt, further confirming the better activity of these MMNCs compared with the Pt control sample. Through Tafel analysis (Fig. 4*C*), slightly smaller Tafel slopes for the MMNCs (32 and 31 mV/decade) were measured, as compared with Pt (37 mV/decade), indicating a similar reaction mechanism in ORR. We also compared our result with the literature data, and our MMNCs are still among best-performing catalysts (*SI Appendix*, Table S3) (43–47).

We also performed rotating ring-disk measurement with a small ring current, and the overall ORR electron number was confirmed to be 3.9~4.0 toward a total oxygen reduction (*SI Appendix*, Fig. S17). In addition, the long-term stability of the as-prepared catalysts was tested by chronoamperometry at 0.6 V (vs. RHE) (Fig. 4*D*). The current density of PtPdRhNi decreased by 36% upon 15-h operation; slightly better activity retention (decreased by 29% after operation for 15 h) was measured for PtPdFeCoNi. In contrast, the current density of Pt decreased by 39.1% after the same time period, during which most activity loss occurred within the first 1 h.

Therefore, the ORR measurements in the RDE configuration verified the excellent catalytic performances and stability of the two screened MMNCs (PtPdRhNi and PtPdFeCoNi), confirming that the knowledge generated by high-throughput discovery is transferrable to conventional testing platforms. Note that due to the complexity of multielement systems, there are no available computational or theoretical tools to fully interpret the high performance of these two compositions out of 22 MMNCs. This would go beyond the scope of the current study. However, the high-throughput synthesis and screening pipeline demonstrated in this work can continuously provide valuable data for future data mining and machine learning for accelerated material discovery.

Conclusion

In this work, we report the high-throughput synthesis of ultrafine and homogeneously alloyed MMNCs through combinatorial composition design by formulating in the precursor solutions followed by rapid thermal shock synthesis. The surface defects on the carbon support are engineered to disperse the MMNCs and ensure size uniformity, while the high-temperature synthesis in the multielement samples with a high entropy largely drives the alloy formation. The uniformity of the MMNCs enables their comparative study for catalytic applications. As an example, we synthesized a series of PtPdRuRhIrFeCoNi MMNCs and rapidly screened for ORR using scanning droplet cell analysis, with two catalysts discovered and

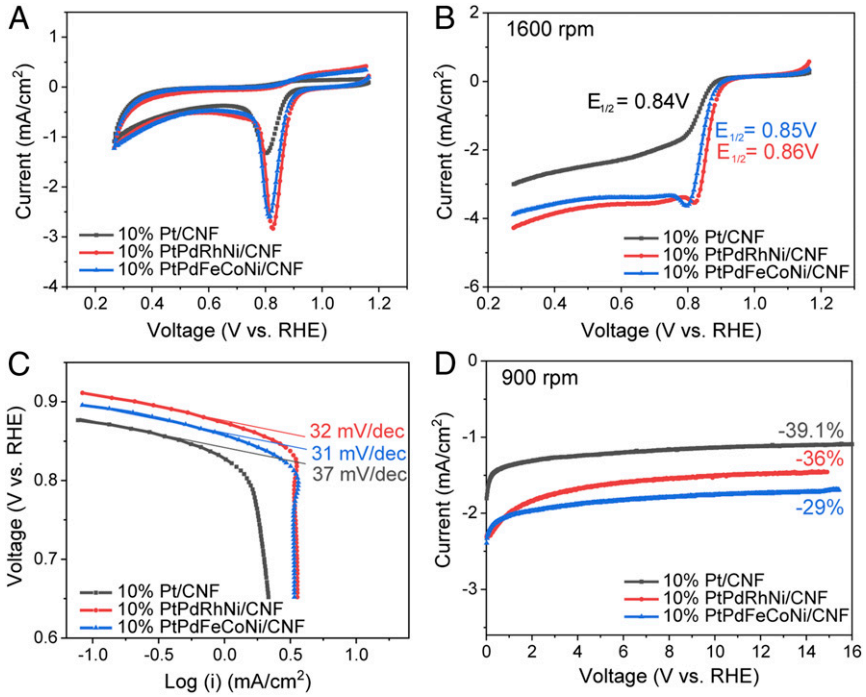

Fig. 4. Electrochemical analysis of PtPdRhNi, PtPdFeCoNi, and a control Pt catalyst for ORR. (*A*) Cycle voltammograms of the three samples, where they show a clear ORR peak at ∼0.8 V (scan rate: 10 mV/s). (*B*) Linear-sweep voltammograms of the three samples (rotation rate: 1,600 rpm; scan rate: 10 mV/s). Both MMNCs outperform the Pt control sample with a higher current at given potentials. (*C*) Tafel analysis of the three samples, displaying similar reaction kinetics for the three samples. (*D*) Stability test for the three samples by holding the potential at 0.6 V (vs. RHE, rotation rate: 900 rpm), in which the three samples show relative stability after an initial decay.

validated using the RDE setup. This high-throughput synthesis and screening method provide a route to accelerate the compositional exploration for MMNC study and could inspire data mining and machine learning for the future development of MMNC catalysts.

Methods

Precursor Loading on CNFs. Electrospun polyacrylonitrile nanofibers were stabilized in the air at 533 K for 6 h and then carbonized at 1,173 K for 2 h in argon (untreated CNFs). The CNF films can be further thermally activated at 1,023 K for 2 h in CO_2 atmosphere to create surface defects (CA-CNFs). The individual metal salts or their hydrate forms (from Sigma-Aldrich) were dissolved in ethanol at a concentration of 0.05 mol/L. We added 10% (in volume) of 37% HCl to $PdCl_2$ solution to completely dissolve $PdCl_2$. The salt precursor solution can be loaded onto the suspended CA-CNF film by using a programmable three-dimensional printer (Fisnar catalog no. F4200N) or by using a pipette with a precursor loading of 5 μmol/cm^2. The precursor salts were used at 1:1 molar ratios between each metallic element in the MMNC design.

Thermal Shock Process. The thermal shock process was performed through Joule heating of the precursor-loaded CA-CNF films in an argon-filled glovebox similar to that reported (35). For batch shock processes (thermally shocking several samples at once), the electrical circuit design involved connecting the copper electrodes in series and then thermally shocking all of the samples (six in our experiment) at one time. In order to achieve uniform temperature in these samples in series, the size of the samples should be as close to the same as possible. The temperature was measured as described (48).

Scaled-Up Synthesis on a Two-Dimensional Substrate. The scaled-up synthesis of MMNCs was performed on a copper-foil-wrapped silicon wafer, in which the copper foil acted as the common working electrode for all samples. The combinatorial compositions were designed and formulated in the solution phase by using individual precursor solutions with a concentration of 0.05 mol/L. The mixture solutions were then dropped on the CA-CNF disks (0.3-inch diameter) with a loading of 100 μL/cm^2 (i.e., ∼5 μmol/cm^2). These CA-CNF disks were attached onto the copper foil in a patterned structure by using conductive silver paste on the bottom. A piece of graphitic carbon paper was used as the radiative heating source driven by Joule heating in an Ar-filled glovebox. The carbon paper was put on top of the samples (∼0.5 cm), heated at 2,000 K for 0.5 s, and repeated three times. Then it was moved to the next samples until all of the samples were heated.

Structural Characterization. See *SI Appendix* for structural characterization.

Electrochemical Screening. High-throughput electrochemical characterization was performed by using a scanning droplet cell. Detailed description of the geometry and operation can be found in previous publications (32) and *SI Appendix*. All of the electrochemical tests were performed at room temperature. After moving to a new sample location, 30 s was given to stabilize the contact between the droplet volume and samples. The electrochemical experiments included two 20 mV/s cyclic voltammetry sweeps followed by one 5 mV/s cyclic voltammetry sweep between 1.1 and 0.45 V vs. RHE. The capillary Ag/AgCl electrode reference electrode was flushed with fresh saturated KCl solution every 30 min to avoid possible contamination and RE potential shift. Because the magnitude of the measured current was around 10^{-4} A, the <50 Ohm uncompensated resistance was ignored.

Detailed Electrochemical Evaluation. A Pine Bipotentiostat RDE4 with a glassy carbon RDE (0.196 cm^2) and a rotating ring-disk electrode (0.247 cm^2, collection coefficient 0.37) were used for detailed electrochemical characterization. The two MMNCs (PtPdRhNi and PtPdFeCoNi) and the Pt control were synthesized on CA-CNF with a loading of ∼10 wt% using a thermal shock synthesis. These samples were then prepared into inks for the measurement in 1.0 M KOH at room temperature (22 ± 1 °C). Details are in *SI Appendix*.

Data Availability. All data are available within the main text and *SI Appendix*.

ACKNOWLEDGMENTS. This work was supported by the Maryland Nanocenter, its Surface Analysis Center, and the AIMLab. R.S.-Y. was supported by NSF Division of Materials Research Award 1809439. R.J. thanks the Electrochemistry Branch, Combat Capabilities Development Command Army Research Laboratory for helpful collaboration in electrocatalysis. Y.L. and C.W. were supported by the Young Investigator Program of the Army Research Office (Grant W911 NF-15-1-0123). Scanning droplet cell measurements were

supported by the Office of Science of the US Department of Energy under Award DE-SC0004993. Y.M. thanks Peter Z. Zavalij for his helpful discussion. This research used resources of the Advanced Photon Source, a US Department of Energy (DOE) Office of Science User Facility operated for the DOE Office of Science by Argonne National Laboratory under Contract DE-AC02-06CH11357. The identification of any commercial product or trade name does not imply endorsement or recommendation by the National Institute of Standards and Technology.

1. Z. Niu *et al*., Anisotropic phase segregation and migration of Pt in nanocrystals en route to nanoframe catalysts. *Nat. Mater.* **15**, 1188–1194 (2016).
2. J. L. Fenton, B. C. Steimle, R. E. Schaak, Tunable intraparticle frameworks for creating complex heterostructured nanoparticle libraries. *Science* **360**, 513–517 (2018).
3. M. Jouny, W. Luc, F. Jiao, High-rate electroreduction of carbon monoxide to multi-carbon products. *Nat. Catal.* **1**, 748–755 (2018).
4. G. Chen *et al*., Interfacial effects in iron-nickel hydroxide-platinum nanoparticles enhance catalytic oxidation. *Science* **344**, 495–499 (2014).
5. D. Wang *et al*., Structurally ordered intermetallic platinum-cobalt core-shell nanoparticles with enhanced activity and stability as oxygen reduction electrocatalysts. *Nat. Mater.* **12**, 81–87 (2013).
6. R. Ferrando, J. Jellinek, R. L. Johnston, Nanoalloys: From theory to applications of alloy clusters and nanoparticles. *Chem. Rev.* **108**, 845–910 (2008).
7. K. Ding *et al*., A general synthesis approach for supported bimetallic nanoparticles via surface inorganometallic chemistry. *Science* **362**, 560–564 (2018).
8. M. Takahashi *et al*., Finely controlled multimetallic nanocluster catalysts for solvent-free aerobic oxidation of hydrocarbons. *Sci. Adv.* **3**, e1700101 (2017).
9. B. Zhang *et al*., Homogeneously dispersed multimetal oxygen-evolving catalysts. *Science* **352**, 333–337 (2016).
10. P.-C. Chen *et al*., Polyelemental nanoparticle libraries. *Science* **352**, 1565–1569 (2016).
11. S. G. Kwon *et al*., Heterogeneous nucleation and shape transformation of multicomponent metallic nanostructures. *Nat. Mater.* **14**, 215–223 (2015).
12. R. G. Weiner, M. R. Kunz, S. E. Skrabalak, Seeding a new kind of garden: Synthesis of architecturally defined multimetallic nanostructures by seed-mediated co-reduction. *Acc. Chem. Res.* **48**, 2688–2695 (2015).
13. P. Buchwalter, J. Rosé, P. Braunstein, Multimetallic catalysis based on heterometallic complexes and clusters. *Chem. Rev.* **115**, 28–126 (2015).
14. C. Chen *et al*., Highly crystalline multimetallic nanoframes with three-dimensional electrocatalytic surfaces. *Science* **343**, 1339–1343 (2014).
15. M. R. Buck, J. F. Bondi, R. E. Schaak, A total-synthesis framework for the construction of high-order colloidal hybrid nanoparticles. *Nat. Chem.* **4**, 37–44 (2011).
16. T. A. A. Batchelor *et al*., High-entropy alloys as a discovery platform for electrocatalysis. *Joule* **3**, 834–845 (2019).
17. B. S. Murty, J.-W. Yeh, S. Ranganathan, *High-Entropy Alloys* (Butterworth-Heinemann, Oxford, UK, 2014).
18. T. Löffler *et al*., Discovery of a multinary noble metal-free oxygen reduction catalyst. *Adv. Energy Mater.* **8**, 1802269 (2018).
19. Z. W. Seh *et al*., Combining theory and experiment in electrocatalysis: Insights into materials design. *Science* **355**, eaad4998 (2017).
20. E. Reddington *et al*., Combinatorial electrochemistry: A highly parallel, optical screening method for discovery of better electrocatalysts. *Science* **280**, 1735–1737 (1998).
21. B. Jandeleit, D. J. Schaefer, T. S. Powers, H. W. Turner, W. H. Weinberg, Combinatorial materials science and catalysis. *Angew. Chem. Int. Ed. Engl.* **38**, 2494–2532 (1999).
22. H. Koinuma, I. Takeuchi, Combinatorial solid-state chemistry of inorganic materials. *Nat. Mater.* **3**, 429–438 (2004).
23. M. Prochaska *et al*., High throughput screening of electrocatalysts for fuel cell applications. *Rev. Sci. Instrum.* **77**, 054104 (2006).
24. W. C. Choi, J. D. Kim, S. I. Woo, Quaternary Pt-based electrocatalyst for methanol oxidation by combinatorial electrochemistry. *Catal. Today* **74**, 235–240 (2002).
25. D. Farrusseng, High-throughput heterogeneous catalysis. *Surf. Sci. Rep.* **63**, 487–513 (2008).
26. R. Potyrailo *et al*., Combinatorial and high-throughput screening of materials libraries: Review of state of the art. *ACS Comb. Sci.* **13**, 579–633 (2011).
27. E. Antolini, Evaluation of the optimum composition of low-temperature fuel cell electrocatalysts for methanol oxidation by combinatorial screening. *ACS Comb. Sci.* **19**, 47–54 (2017).
28. T. S. Almeida, A. R. Van Wassen, R. B. VanDover, A. R. de Andrade, H. D. Abruña, Combinatorial PtSnM (M = Fe, Ni, Ru and Pd) nanoparticle catalyst library toward ethanol electrooxidation. *J. Power Sources* **284**, 623–630 (2015).
29. E. J. Kluender *et al*., Catalyst discovery through megalibraries of nanomaterials. *Proc. Natl. Acad. Sci. U.S.A.* **116**, 40–45 (2019).
30. Y. Yao *et al*., Ultrafast, controllable synthesis of sub-nano metallic clusters through defect engineering. *ACS Appl. Mater. Interfaces* **11**, 29773–29779 (2019).
31. J. H. Zhou *et al*., Characterization of surface oxygen complexes on carbon nanofibers by TPD, XPS and FT-IR. *Carbon* **45**, 785–796 (2007).
32. J. A. Haber *et al*., Discovering Ce-rich oxygen evolution catalysts, from high throughput screening to water electrolysis. *Energy Environ. Sci.* **7**, 682–688 (2014).
33. Y. Yao *et al*., High temperature shockwave stabilized single atoms. *Nat. Nanotechnol.* **14**, 851–857 (2019).
34. L. Huang *et al*., Catalyst design by scanning probe block copolymer lithography. *Proc. Natl. Acad. Sci. U.S.A.* **115**, 3764–3769 (2018).
35. Y. Yao *et al*., Carbothermal shock synthesis of high-entropy-alloy nanoparticles. *Science* **359**, 1489–1494 (2018).
36. P. Xie *et al*., Highly efficient decomposition of ammonia using high-entropy alloy catalysts. *Nat. Commun.* **10**, 4011 (2019).
37. J. M. Gregoire, C. Xiang, X. Liu, M. Marcin, J. Jin, Scanning droplet cell for high throughput electrochemical and photoelectrochemical measurements. *Rev. Sci. Instrum.* **84**, 024102 (2013).
38. J. M. Gregoire, R. B. van Dover, J. Jin, F. J. Disalvo, H. D. Abruña, Getter sputtering system for high-throughput fabrication of composition spreads. *Rev. Sci. Instrum.* **78**, 072212 (2007).
39. J. Li *et al*., Combinatorial screening of Pd-based quaternary electrocatalysts for oxygen reduction reaction in alkaline media. *J. Mater. Chem. A* **5**, 67–72 (2017).
40. L. Dai, Y. Xue, L. Qu, H. J. Choi, J. B. Baek, Metal-free catalysts for oxygen reduction reaction. *Chem. Rev.* **115**, 4823–4892 (2015).
41. K. Shinozaki, J. W. Zack, R. M. Richards, B. S. Pivovar, S. S. Kocha, Oxygen reduction reaction measurements on platinum electrocatalysts utilizing rotating disk electrode technique: I. Impact of impurities, measurement protocols and applied corrections. *J. Electrochem. Soc.* **162**, F1144–F1158 (2015).
42. C. A. Campos-Roldán, R. G. González-Huerta, N. Alonso-Vante, Experimental protocol for HOR and ORR in alkaline electrochemical measurements. *J. Electrochem. Soc.* **165**, J3001–J3007 (2018).
43. Y. Liang *et al*., Co_3O_4 nanocrystals on graphene as a synergistic catalyst for oxygen reduction reaction. *Nat. Mater.* **10**, 780–786 (2011).
44. S. Mao, Z. Wen, T. Huang, Y. Hou, J. Chen, High-performance bi-functional electrocatalysts of 3D crumpled graphene-cobalt oxide nanohybrids for oxygen reduction and evolution reactions. *Energy Environ. Sci.* **7**, 609–616 (2014).
45. A. Hernández-Ramírez *et al*., Evaluation of the nickel titanate-modified Pt nanostructured catalyst for the ORR in alkaline media. *J. Electrochem. Soc.* **163**, F16–F24 (2016).
46. L. Wang *et al*., Co@Pt Core@Shell nanoparticles encapsulated in porous carbon derived from zeolitic imidazolate framework 67 for oxygen electroreduction in alkaline media. *J. Power Sources* **343**, 458–466 (2017).
47. N. Zhang *et al*., High Pt utilization efficiency of electrocatalysts for oxygen reduction reaction in alkaline media. *Catal. Today* **332**, 101–108 (2019).
48. R. J. Jacob, D. J. Kline, M. R. Zachariah, High speed 2-dimensional temperature measurements of nanothermite composites: Probing thermal vs. gas generation effects. *J. Appl. Phys.* **123**, 115902 (2018).